

RICE UNIVERSITY

**Imaging Plasmons with Compressive Hyperspectral
Microscopy**

by

Liyang Lu


A THESIS SUBMITTED
IN PARTIAL FULFILLMENT OF THE
REQUIREMENTS FOR THE DEGREE

Master of Science

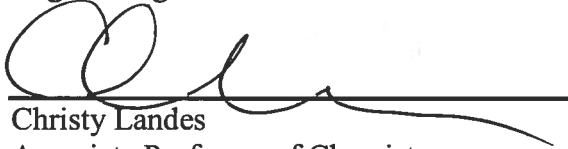
APPROVED, THESIS COMMITTEE



Kevin F. Kelly, Chair
Associate Professor of Electrical and
Computer Engineering



Richard G. Baraniuk
Victor E. Cameron Professor of
Engineering



Christy Landes
Associate Professor of Chemistry

HOUSTON, TEXAS

May 2015

ABSTRACT

Imaging Plasmons with Compressive Hyperspectral Microscopy

by

Liyang Lu

With the ability of revealing the interactions between objects and electromagnetic waves, hyperspectral imaging in optical microscopy is of great importance in the study of various micro/nano-scale physical and chemical phenomena. The conventional methods, however, require various scanning processes to acquire a complete set of hyperspectral data because of its 3-dimensional structure. As such the quality and efficiency of the data acquisition using these conventional scanning techniques is greatly limited by the detector sensitivity and low signal light intensity from the sample. To overcome such limitations, we applied compressive sensing theory to the hyperspectral imaging. The compressive imaging enhances the measurement signal-to-noise ratio by encoding and combining the spatial information of the sample to the detector, and a recovery algorithm is used to decode the detector outputs and reconstruct the image. A microscopy system based on this compressive hyperspectral imaging scheme was designed and implemented. Further analysis and discussion on the diffraction and interference phenomenon and a solution to the spectral distortion in this compressive sensing microscopy system are also presented. Experimental results of compressive dark-field scattering from gold nanobelts are presented,

followed with an analysis on signal-to-noise ratio and a comparison with conventional scanning methods in measuring the plasmon resonances.

Acknowledgments

I'm using this opportunity to express my sincere gratitude to my advisor Professor Kevin Kelly for his invaluable support given to me throughout the course of my research, for his patience, motivation, and knowledge that are guiding me in the realm of compressive imaging and nanotechnology.

I would also like to thank Professor Richard Baraniuk and Professor Christy Landes for serving as my thesis committee members, and for their brilliant comments and suggestions.

I thank all my group mates in SPC lab and STM lab for their support in research and life. I want to thank Dr. Lina Xu and Yun Li in particular for their guidance since the first day I joined the group. Also I thank my collaborators Prof. Jason Hafner and Dr. Lindsey Anderson for providing me the experiment samples.

My sincere thanks also go to Dr. Kathrin Berkner and her group for offering me the summer internship opportunity and leading me on the exciting project.

Last but not least, I would like to thank my family for their selfless love and unconditional support throughout these years.

Contents

Abstract	ii
Acknowledgments.....	iv
Contents	v
List of Figures	vii
1. Introduction	1
1.1. Hyperspectral Microscopy.....	1
1.2. Surface Plasmon Resonance Scattering Spectrum.....	4
1.3. Scope	5
2. Compressive Imaging Theory	6
2.1. Sampling and Imaging	6
2.2. Compressive Sensing.....	8
2.2.1. CS Measurement	8
2.2.2. CS Reconstruction.....	10
2.3. Single-Pixel Camera	11
3. Compressive Hyperspectral Microscopy	14
3.1. Compressive Hyperspectral Microscopy System Design	15
3.1.1. Scattering Microscopy of Plasmonic Nanostructures	16
3.1.2. Spatial Light Modulation and Spectrum Measurement	17
3.2. Hyperspectral Data Measurement and Reconstruction	18
3.2.1. Compressive Sensing of the Hyperspectral Data	18
3.2.2. Hyperspectral Data Reconstruction.....	20
3.3. DMD Diffraction and Interference	21
4. Experimental Results	27
4.1. 1951 USAF Standard Microscope Resolution Target	27
4.2. Hyperspectral Imaging of Nanostructure Surface Plasmon Scattering.....	29
4.3. Noise Analysis.....	33
4.4. Comparison between Compressive Imaging and Raster Scanning	36
5. Conclusion and Future Work.....	42

References	44
-------------------------	-----------

List of Figures

Figure 1.1 Cartoons of a hyperspectral data cube (left) and three conventional data acquisition methods (right) [11]	2
Figure 2.1 CS measurement of a sparse signal under the representation basis Ψ , cited from [22]	9
Figure 2.2 Schematic diagram of the single-pixel camera [36].....	12
Figure 3.1 (a) Schematic layout of the compressive hyperspectral microscopy system. (b) Detailed structure of two micromirrors at different states. (c) Configuration of the nanoparticle sample.	16
Figure 3.2 A 1024-pixel (32×32) binary pattern formed by one row of the pseudo-randomly permuted 1024×1024 Walsh-Hadamard matrix	20
Figure 3.3 The simulated magnitude (left) and phase (right) of a diffraction-limited spot at 530-nm wavelength on the image plane after being reflected by the +12°-tilted micro-mirrors.....	22
Figure 3.4 The spectra of (a) a copper reference grid, and (b) a sample of silver nanowires that are affected by the interference	22
Figure 3.5 The simulated focused spots formed on the Fourier plane of the image at (a) 530-nm, (b) 560-nm, and (c) 590-nm wavelengths, using unmodified DMD patterns; (d) the focused spot formed by a combination of 10 discrete wavelengths between 400 nm and 700 nm, using unmodified DMD patterns; the focused spots at (e) 530-nm, (f) 560-nm, and (g) 590-nm wavelengths, formed by modified DMD patterns; and (h) the focused spot formed by a combination of 10 discrete wavelengths between 400 nm and 700 nm, using modified DMD patterns. The red circles indicate the the region of the fiber end.....	24
Figure 3.6 A modified 1024-pixel (32×32) binary pattern with an additional striped modulation pattern.....	25
Figure 3.7 The spectra of (a) a copper reference grid, and (b) a sample of silver nanowires measured with modified DMD patterns.....	26

Figure 4.1 A 1951 USAF resolution target is imaged at 16384-pixel (128×128) resolution with the compressive hyperspectral microscopy system. The image slice at 637.44-nm wavelength is reconstructed at different sampling ratios. (a) A full set of compressive measurement results at 637.44-nm wavelength with a bandwidth of 1.52 nm. (b) The peak signal-to-noise ratio (PSNR) of the recovered images as a function of the sampling ratio (M/N). The insets show the images recovered from 10%, 25%, and 50% of the total measurements..29

Figure 4.2 Examples of the reconstructed hyperspectral data of the gold nanobelt plasmon scattering at 25% sampling ratio. On top left of each subfigure is the cropped CMOS camera image showing the nanobelt of interest. The reconstructed spectra of 10 points along the nanobelt are plotted on top right. And on the bottom of each subfigure are six synthesized single-band image slices from the reconstructed hyperspectral data cube.....32

Figure 4.3 The reconstructed spectra from the measurements with different integration time. (a) CMOS camera image of the gold nanobelt. The red circle highlights the point where the spectra are plotted. (b) The reconstructed spectra of the high-lighted point with 100-ms, 50-ms, 25-ms, and 10-ms integration time. (c) The reconstructed spectra normalized to their own maximum values.36

Figure 4.4 The single band images of the gold nanobelt sample at 550-nm wavelength acquired with CS and raster-scanning hyperspectral imaging methods.....40

Figure 4.5 The spectra on pixel (18, 30) of the hyperspectral data cube acquired with CS and raster-scanning methods at the 64×64 resolution. The spectrometer integration time is 25 ms.41

Chapter 1

Introduction

1.1. Hyperspectral Microscopy

Hyperspectral imaging in optical microscopy is of great importance in the study of various micro/nano-scale physical and chemical phenomena. By investigating the response of a specimen to electromagnetic waves as a function of both spatial position and wavelength, hyperspectral microscopy enables people to achieve abundant information from the 3D spatial-spectral structure of the specimen. It has been proved to be a powerful and effective technique in analyzing plasmonic scattering spectra of metal nanostructures [1-3], the emission spectra of fluorescent molecules in biomedical samples [4, 5], and in other applications[6, 7].

However, the practical use of hyperspectral imaging is yet limited in several aspects. As a digital imaging technique, conventional hyperspectral microscopy is also in the regime of the Shannon-Nyquist sampling theorem. The bandwidth of the

information that can be captured by the sensor, be stored, and be represented by digital data is determined by the number of sampling points. Because of the fact that hyperspectral data has 3-dimensions, 2 spatial dimensions and one additional dimension in spectral domain, in order to achieve a detailed spatial-spectral structure of the object, both the spatial resolution and the spectral resolution are required to be sufficiently high. This additional spectral dimension increases the amount of sampling points that need to be independently measured by several orders of magnitudes.

In addition, there is no off-the-shelf “hyperspectral sensor” to directly capture the 3D hyperspectral data. In conventional methods, a one-dimensional or two-dimensional detector array needs to scan either in the spatial dimensions [8, 9], or in the spectral dimension [10] to get the 3D data, as shown in Figure 1.1. This makes the whole data acquisition process time consuming and pushes the limit in terms of detector sensitivity.

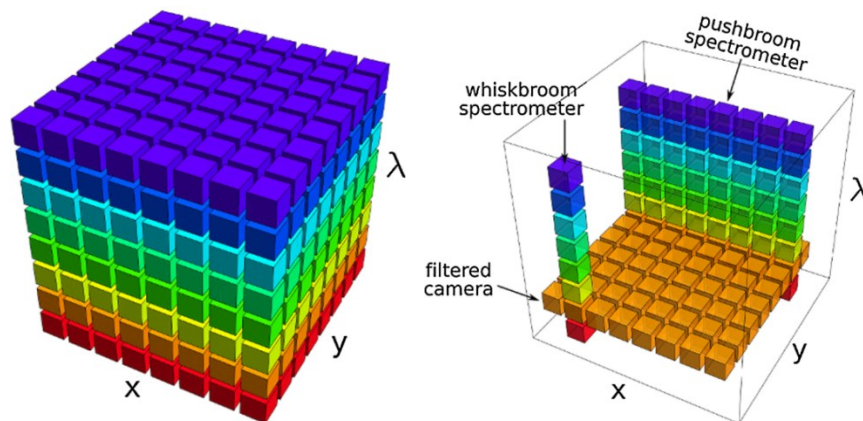


Figure 1.1 Cartoons of a hyperspectral data cube (left) and three conventional data acquisition methods (right) [11]

With the conventional scanning methods, each element of the detector array can only receive the signal photons from one pixel of the image and within one spectral band. The signal to noise ratio reduces significantly with an increase of the image resolution, so a much longer integration time or a high sensitivity detector array, such as EMCCD [12, 13] and sCMOS [13], is required to compensate for the reduction of signal photons.

Recently, multiple novel hyperspectral and multispectral imaging schemes have been proposed to achieve greatly improved data acquisition efficiency, including filter stack spectral decomposition (FSSD) [14], coded aperture snapshot spectral imaging (CASSI) [15], image mapping spectroscopy (IMS) [16], and Image Slicing Spectrometer (ISS) [17]. Yet these methods introduced additional restrictions on wavelength range, spectral variety, spatial resolution, and spectral resolution [11]. The filter stack used in FSSD can only provide a limited number (less than 10) of spectral bands due to filter losses. In CASSI, the recovery of the hyperspectral data from spatially coded and spectrally dispersed images trades off among spatial resolution, spectral resolution, and accuracy of the estimation. IMS/ISS requires the use of a custom image mapping array and a precision lens array, as well as a detector array with a large amount of pixels to capture the whole spatial-spectral data at the same time. In addition, when imaging beyond the visible spectrum, these methods will be expensive as they all require 2-D arrays of detectors other than silicon.

1.2. Surface Plasmon Resonance Scattering Spectrum

Surface plasmon resonance (SPR) is a phenomenon that strong collective oscillations of the electrons occur when nanoparticles are stimulated by incident light at or near the nature frequency of the surface electron oscillation. Gold and silver nanostructures with subwavelength dimensions have been widely studied for their ability to form localized SPR when excited by light at visible and infrared frequencies. Because of their tunability, sharp resonance, strong field localization and enhancement, these noble metal plasmonic nanoparticles have found novel applications in a wide variety of fields such as medical science, solar energy harvest, nanophotonics, and etc. [18-20]. After new metal nanostructures are synthesized or fabricated, an essential step is to characterize their true plasmonic resonance frequencies. As the SPR wavelength is closely related to the shape and dimensions of a nanoparticle, it is also necessary to study the structure-spectrum correspondence by investigating the plasmon resonance of each individual nanoparticle.

When the nanoparticles are excited with a wide band illumination, the light around the plasmon resonance wavelength is absorbed to excite the collective electron oscillations on the nanoparticles. These strong electron charge oscillations or plasmon resonances not only lead to a near-field enhancement, but also interact with the incident EM wave and cause an enhanced far-field scattering, of which the spectra are directly related to the SPR frequencies. A scattering microscope can avoid the transmitted and reflected light from the nanoparticles and only collect the scattered light caused by the plasmon resonances, enabling us to characterize the

SPR properties of the nanoparticles. The scattering hyperspectral microscopy is an especially useful technique for the characterization of individual plasmonic nanoparticles as it is able to acquire a comprehensive set of 3D spatial-spectral data of the sample within the field of view.

1.3. Scope

In this thesis, we present a new hyperspectral microscopy system based on the theory of compressive sensing that tackles the efficiency problem of hyperspectral imaging and enhances the signal-to-noise ratio by randomly encoding the image and multiplexing the spectral detection.

In Chapter 2, we will review the theory of compressive sensing, and will introduce the single-pixel camera, a unique hardware implementation of compressive imaging system with a single-element detector.

In Chapter 3, the proposed compressive hyperspectral microscopy system will be described in detail. The DMD diffraction, which largely affects the measured spectra, and our solution to the problem will be discussed.

In Chapter 4, the experimental results with surface plasmon nanostructures will be presented. The noises in the system will be analyzed. We will also compare our results with raster-scanning methods at various resolutions to show the advantage of the compressive imaging scheme.

Chapter 2

Compressive Imaging Theory

Compressive sensing (CS), also known as compressive sampling or compressed sensing, is a potential method to tackle the limit of the Nyquist sampling frequency. Compared to the conventional sampling methods, it provides greatly improved efficiency in the acquisition of high-dimensional data. The work of Emmanuel Candes, Justin Romberg, Terence Tao, and independently David Donoho has proved that if high-dimensional signals have sparse or compressible representations, they could be reconstructed from a set of measurements fewer than being required by the Shannon-Nyquist theorem [21-24].

2.1. Sampling and Imaging

In order to convert the real world signal into a digital form for efficient storage, transmission, and analysis without losing important information conveyed,

a correct sampling of the signal is the first and one of the most crucial steps in the signal processing.

Applying conventional sampling method on a signal $s(t)$ can be simply represented as:

$$s_k = s(kT),$$

where k is an integer, and T is a constant sampling interval. Only the values at the moments kT of the original signal are recorded while the rest are lost. According to the Shannon-Nyquist sampling theorem, for a band-limited signal, the sampling rate $1/T$ needs to be at least twice of the signal bandwidth in order to avoid any loss of the information in the original continuous signal after the sampling.

The amount of data generated by sampling complicated and/or high-dimensional signals, e.g. images and videos, can be extraordinarily large. The resources, e.g. sensors and time, needed for the acquisition of the data also increase quickly with its size. The conventional Nyquist sampling method cannot address the dilemma caused by the limited resources we have and the highly detailed physical world we want to capture.

2.2. Compressive Sensing

2.2.1. CS Measurement

Sparsity in and compressibility of various signals has been exploited in different ways during the long history of the development of digital signal processing. By using proper designs of sparse representation dictionaries of the signals, such as Fourier transform, discrete cosine transform (DCT), and wavelet transform, the efficient storage and transmission of large images, sound tracks, and videos were made possible. In conventional sampling schemes, original data are completely measured and then compressed into formats such as JPEG, MP3 and MPEG.

Compressive sensing, however, performs the signal compression within the procedure of measurement. Using CS, a compressible original signal can be approximated very accurately with far fewer measurements than what are indicated by its bandwidth [23, 25]. For a length- N k -sparse signal, instead of directly measuring the values of all N samples, compressive sensing takes M ($k < M \leq N$) measurements through a special process that can be mathematically modeled by

$$\mathbf{y} = \Phi \mathbf{x} \quad 1.1$$

where Φ is an $M \times N$ measurement matrix, \mathbf{x} is the length- N unknown signal vector being measured, and \mathbf{y} is a length- M vector containing M measured values. If the original signal vector is not sparse under the standard basis but can be sparsely

represented under some other transform basis, the measurement process can be expressed by

$$\mathbf{y} = \Phi \mathbf{x} = \Phi \Psi \mathbf{s}. \quad 1.2$$

where Ψ is an $N \times N$ transform matrix, and \mathbf{s} is a length- N sparse vector. Figure 2.1 illustrates this measurement process.

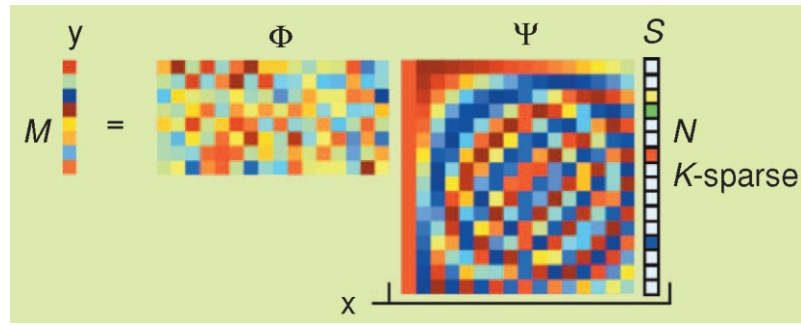


Figure 2.1 CS measurement of a sparse signal under the representation basis Ψ , cited from [22]

An important topic in CS theory is to design a proper incomplete ($M < N$) measurement matrix Φ so that most information in the k -sparse signal can be preserved and reconstructed. The restricted isometry property (RIP) and the condition of incoherence between rows of measurement matrix Φ and sparse representation basis Ψ are proposed as sufficient conditions for a stable solution for k -sparse signals [23, 25, 26]. Although a direct construction of a measurement matrix to satisfy RIP and incoherence is NP-hard, recent research has shown that both conditions can be achieved with high probability by a random matrix [27, 28], which also shows properties of democracy [29] and universality[30].

2.2.2. CS Reconstruction

Reconstruction of the length- N signal from M measurements is an ill-posed inverse problem as $M < N$. Among all the infinitely many solutions for it, finding the one that satisfy the prior structural information such as sparsity, denoted by equation 1.3, is numerically unstable and NP-complete [22].

$$\hat{\mathbf{s}} = \arg \min \|\mathbf{s}\|_0, \text{ s.t. } \Phi\Psi\mathbf{s} = \mathbf{y} \quad 1.3$$

An l_1 -norm optimization alternative, as shown in equation 1.4, provides a surprisingly good approximation to the sparse solutions, and can be reduced to a linear program with computational complexity of about $O(N^3)$ [23, 25]. The equivalence of l_1 minimization and l_0 minimization on signal recovery under some conditions has been theoretically proved by Candes, Tomberg, Tao, and Donoho [23, 25, 27]. It is also known as Basis Pursuit, and is widely used in solving the CS reconstruction problems.

$$\hat{\mathbf{s}} = \arg \min \|\mathbf{s}\|_1, \text{ s.t. } \Phi\Psi\mathbf{s} = \mathbf{y} \quad 1.4$$

In the field of CS image reconstruction, total variation (TV) regularization is another well-known method for its ability to recover the edges or boundaries more accurately than l_1 method. TV minimization suggests that the gradient of the 2D image signal is sparse, so it can be considered as a generalized l_1 minimization problem on the image gradient map. It can be expressed as

$$\hat{\mathbf{x}} = \arg \min \sum_i \|D_i \mathbf{x}\|, \text{ s.t. } \Phi \mathbf{x} = \mathbf{y} \quad 1.5$$

where $\|D_i \mathbf{x}\|$ is the discrete gradient magnitude at pixel i of the image \mathbf{x} .

Multiple TV minimization solvers have been proposed, including SOCP [31], TwIST [32], NESTA [33], and TVAL3 [34]. In this thesis, we use TVAL3 as our CS image reconstruction solver.

2.3. Single-Pixel Camera

As a demonstration of the application of compressive sensing theory in the field of imaging, the single-pixel camera (SPC) was proposed and successfully implemented recently by Baraniuk, Kelly, et al. [35]. It tackles the inefficiencies and bandwidth limits in conventional digital imaging systems by combining the image compression into the imaging processes.

In a conventional imaging system, a photodetector array is used to sample the optical information and to convert it into an array of numbers proportional to the light intensities the detectors receive. To get an image with N pixels, a detector array with at least N elements is needed. The spatial sampling rate or the resolution of the captured image is limited by the amount of the sensing elements in the system. Then the image would be compressed into a format such as JPEG for efficient storage and transmission. This “compression after imaging” approach causes a waste of the imaging resources.

In addition, the detection of the light beyond the visible spectrum, e.g. short wave infrared (SWIR) and mid-wave infrared (MWIR), requires special non-silicon-based sensing devices. A high-resolution array of these detectors can be very expensive. An alternative scheme of imaging is therefore needed for these special applications.

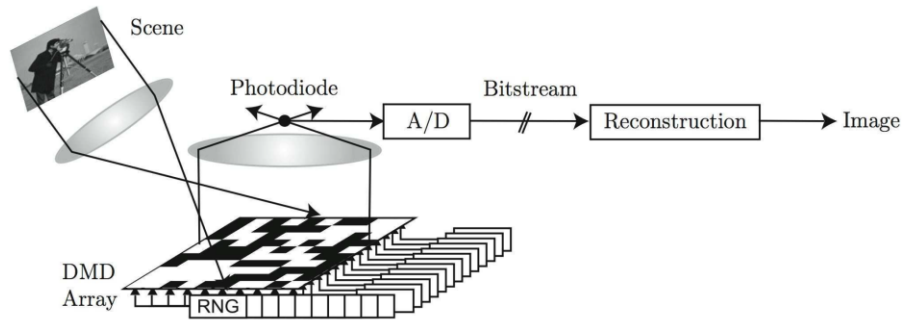


Figure 2.2 Schematic diagram of the single-pixel camera [36]

The design of the single-pixel camera is aimed to solve these shortages of the conventional imaging scheme. It consists of a digital micro-mirror device (DMD), a photodiode, and multiple basic optical components, as shown in Figure 2.2. The DMD performs as a spatial light modulator that encodes the image of the scene projected on it with the pseudorandom patterns defined by the rows of the designed modulation matrix Φ . The light of the modulated image is then converged by lenses to the photodiode. The photodiode output is recorded for each of M modulation patterns, and all M outputs compose the length- M measurement vector y in equation 1.1. From these M measurements and their corresponding patterns, the

original image with $N(>M)$ pixels can finally be recovered using proper reconstruction algorithms described in the previous section.

Compressive Hyperspectral Microscopy

In this chapter, we present a hyperspectral microscopy scheme based on compressive sensing, and demonstrate the experimental results by studying surface plasmon resonance scattering spectra of metal nanostructures. Using this system, the total amount of measurements can be greatly reduced without losing detail in the 3D hyperspectral data cube thanks to the nature of compressive sensing. An enhancement in sensitivity is also achieved as the spectrometer in our system is always receiving about 50% of the total light from the sample in every measurement, regardless of the actual pixel size or the target image resolution. The combination of hyperspectral microscopy with the features of compressive imaging, such as fast, high dynamic range, and enhanced signal-to-noise ratio (SNR), gives us a powerful and low-cost spectral analytical system in the field of nanotechnology. This approach is also more easily extended to wavelength beyond the visible spectrum than other alternatives.

3.1. Compressive Hyperspectral Microscopy System Design

The technique of CS features its ability of reconstructing a signal from fewer measurements than what are indicated by its bandwidth. In order to acquire the hyperspectral data using CS, we encode the image by projecting it onto a series of spatial measurement vectors. It is realized by using a DMD as a spatial light modulator (SLM) to modulate the intensities of the image pixels with the specially designed binary patterns on it, and lenses are used to focus and couple the modulated light into an optic fiber, which guides the encoded light signal into a spectrometer for the spectrum extraction.

The schematic layout of the designed system is illustrated in Figure 3.1 (a). The whole setup can be considered to be composed of two major parts, of which one is an optical magnification part, and the other is an image modulation and spectrum measurement part. These two parts will be introduced in detail in the following sections. As the optical magnification and the image modulation are two independent steps, the same model can be easily applied to different types of optical microscopes by only changing the optical magnification part or adapting the image modulation and measurement part to commercial optical microscopes. In our experiments, in order to image the SPR scattering from metal nanostructures, the optical magnification part is set up as a scattering microscopy system. In addition to these two major parts, a CMOS camera is used to monitor the position of the sample and the focusing condition of the image on the DMD.

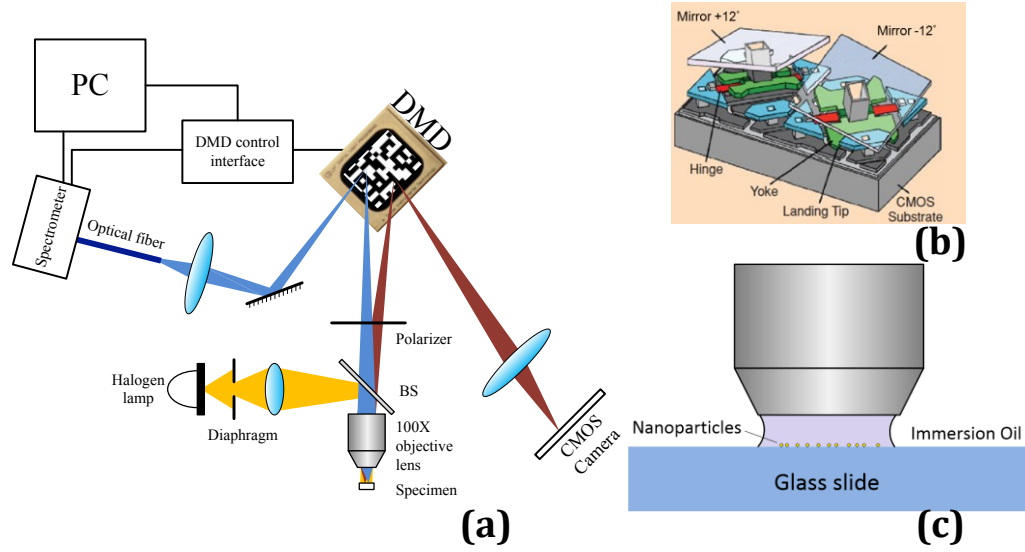


Figure 3.1 (a) Schematic layout of the compressive hyperspectral microscopy system. (b) Detailed structure of two micromirrors at different states. (c) Configuration of the nanoparticle sample.

3.1.1. Scattering Microscopy of Plasmonic Nanostructures

The optical magnification part of our setup is essentially a scattering microscopy system. It consists of a 3-axis stage for sample positioning, a 100X finite conjugate oil immersive objective lens (LABOMED LP-Series DIN 100X/ NA 1.25/ WD 0.17 semi-plan achromatic lens), a halogen lamp, and a polarizer, as shown in Figure 3.1.

The samples for microscopic imaging were prepared by depositing the plasmonic metal nanoparticles on glass substrates. The halogen lamp illuminates the sample through the objective lens with the help of a 45° non-polarizing beam-splitter (BS). The Kohler illumination design is used to achieve an evenly distributed illumination on the sample. By applying index-matching immersion oil between the

sample and the lens, as illustrated in Figure 3.1 (c), the reflection from the interfaces is mostly reduced, and at the same time, a high numerical aperture ($NA=1.25$) can be achieved to capture a larger portion of the scattered light. For the samples of metal nanostructures that are on the dimensions much less than the wavelength, the majority of the signal going through the objective and received by the detector is the scattered light from the nanostructures. Consequently, the recovered images will be similar to the dark-field scattering images. A polarizer is utilized and adjusted according to the orientation of the nanostructure of interest for the observation of specific linearly polarized light from the sample.

3.1.2. Spatial Light Modulation and Spectrum Measurement

To realize the image modulation, a Texas Instrument (TI) DMD chip is incorporated at the image plane of the sample. The functional part of the DMD is a 768×1024 array of electrostatically controlled micro-mirrors of size 13.68×13.68 μm each. Every micro-mirror can be independently actuated by an individual SRAM cell, and rotate about a hinge to be at one of two states, $+12^\circ$ (tilting left) and -12° (tilting right) with respect to the DMD surface, as shown in Figure 3.1 (b). The DMD is in the plane orthogonal to the optical axis of the magnification part, and is rotated 45° so the hinges are all in vertical direction. As a result, all the micro-mirrors oriented at $+12^\circ$ reflect the parts of image on them at an angle around $+24^\circ$ (twice the tilting angle), toward the light collecting lens and the OceanOptics QE65000 spectrometer on the left for the spectrum measurement. Because the acceptance angle of the fiber is limited by its numerical aperture, the focal length of the light

collecting lens is designed to make sure the light from the whole field of view of the microscope can be coupled into the fiber at the focal point. In our setup, the focal length of the light collecting lens is chosen to be 50 mm for the visible-NIR fiber with a core diameter of 0.6 mm and a numerical aperture of 0.22. The micro-mirrors oriented at -12° , on the other hand, project the light on them toward the monitoring CMOS camera at -24° . These two cases are indicated in Figure 3.1 with blue and red rays respectively. Because the detector (or spectrometer) only receives the light from the micro-mirrors tilting left ($+12^\circ$) in each measurement, we indicate left-tilting micro-mirrors with white color. And the rest of the micro-mirrors are in black.

The spectrometer integration measurements are synchronized with the changes of the patterns on the DMD using a trigger signal from the DMD control interface. In this way, we can correctly match every spectrometer output with the corresponding DMD pattern.

3.2. Hyperspectral Data Measurement and Reconstruction

3.2.1. Compressive Sensing of the Hyperspectral Data

Using the hardware system described in Section 3.1, the customized DMD control program, and the spectra data collection software SpectraSuite, we can perform the compressive sensing on the hyperspectral data of the microscopic samples. During the measurement process, the DMD displays a series of binary patterns by flipping the micro-mirrors, and the spectrometer records one spectrum

for each DMD pattern. In each spectrum measurement, the signal received by the spectrometer is the inner product of the image intensity distribution and the binary DMD pattern.

The hyperspectral compressive measurement process can be modeled as

$$\mathbf{Y} = \Phi \mathbf{X}, \quad 2.1$$

which is similar to equation 1.1. Φ is the $M \times N$ measurement matrix, with each row a measurement vector ϕ_m that defines one modulation pattern on the DMD. Here, \mathbf{X} is the $N \times K$ unknown hyperspectral data matrix being measured. Each column of \mathbf{X} is a vectorized N -pixel image at a single band, and the whole matrix contains K different spectral bands. \mathbf{Y} is an $M \times K$ matrix containing the measurement results. The rows of matrix \mathbf{Y} are the spectra recorded by the spectrometer for M different measurements.

The binary DMD patterns are defined by the rows of the measurement matrix Φ . To capture an N -pixel image, we use M rows from a pseudo-randomly permuted $N \times N$ Walsh-Hadamard matrix as the measurement vectors. The pseudo-random binary patterns have been proven to be highly incoherent with the sparse bases of most natural images, making them suitable for the CS applications. As an example, Figure 3.2 displays a 1024-pixel (32×32) binary DMD pattern formed by one row of the pseudo-randomly permuted 1024×1024 Walsh-Hadamard matrix. The pattern is rotated 45° in accordance with the actual pose of the DMD chip.



Figure 3.2 A 1024-pixel (32×32) binary pattern formed by one row of the pseudo-randomly permuted 1024×1024 Walsh-Hadamard matrix

In our experiments, we imaged the samples at the resolutions of 4096-pixel (64×64) and 16384-pixel (128×128), by grouping every 12×12 or 6×6 micro-mirror array on the DMD together as a “one-pixel” patch.

3.2.2. Hyperspectral Data Reconstruction

The reconstruction process recovers the unknown hyperspectral data matrix \mathbf{X} from the measurement outputs in \mathbf{Y} . The algorithm used for the reconstruction is TVAL3, and we slightly modified it to adapt to the hyperspectral data application. It solves the compressive sensing problem with total variation regularization in the spatial dimensions:

$$\hat{\mathbf{X}} = \arg \min \sum_k \sum_i \|D_i \mathbf{X}[:, k]\|, \text{ s.t. } \Phi \mathbf{X} = \mathbf{Y}, \quad 2.2$$

where $D_i \mathbf{X}[:, k]$ is the discrete spatial gradient vector of the image at the spectral band k and pixel i .

3.3. DMD Diffraction and Interference

In our high-magnification microscope setup, DMD diffraction and interference are significant enough to distort the spectra measured by the fiber-coupled spectrometer even with incoherent, visible wavelengths of light. Therefore we engineered the patterns on the DMD to solve the problem.

Due to the large optical magnification of the microscopy system and the diffraction-limited resolution of the objective lens, a spatially coherent spot with a diffraction-limited diameter

$$d_s = \frac{2.44S_i\lambda}{D_a} = 1.22M\lambda \left[\left(\frac{n_0}{NA} \right)^2 - 1 \right]^{1/2} \quad 2.3$$

is formed on the DMD for every point on the sample. D_a is the objective aperture size. S_i is the image distance from the aperture. M here stands for the magnification, and n_0 is the refractive index of the immersion medium between the sample and the objective. For our microscopic setup with the 100X oil-immersion objective lens, d_s is estimated to be 48.55 μm , which is much larger than the dimension of one micro-mirror. Figure 3.3 shows the simulated magnitude and phase of such a diffraction-limited spot at 530-nm wavelength after being reflected by a small array of micro-mirrors. When it is focused at the end of the fiber, interference will occur because the micro-mirrors tilting at $+12^\circ$ cause a periodic phase change on the spot. Consequently, only the wavelengths that are interfering constructively at the fiber end can be coupled into the spectrometer. As shown in Figure 3.4, the early results

of two different samples illuminated by white LED show similar spectra with 4 discrete peaks between 400-nm and 700-nm wavelengths. These peak wavelengths have equally spaced wave numbers, and can be proved to be where the constructive interferences occur.

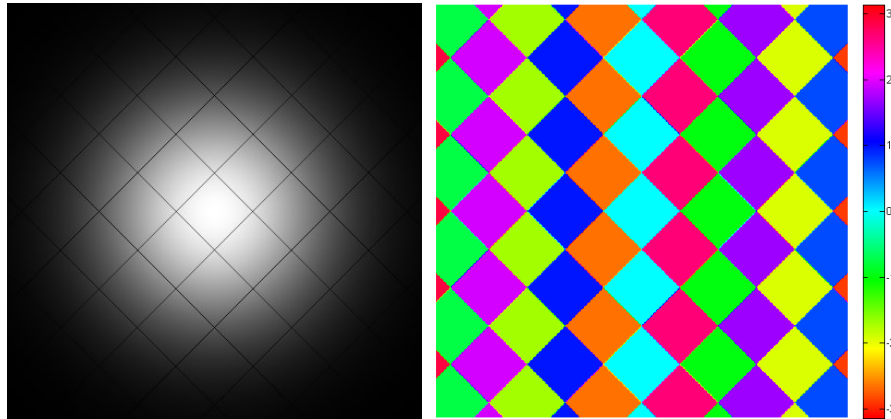


Figure 3.3 The simulated magnitude (left) and phase (right) of a diffraction-limited spot at 530-nm wavelength on the image plane after being reflected by the $+12^\circ$ -tilted micro-mirrors.

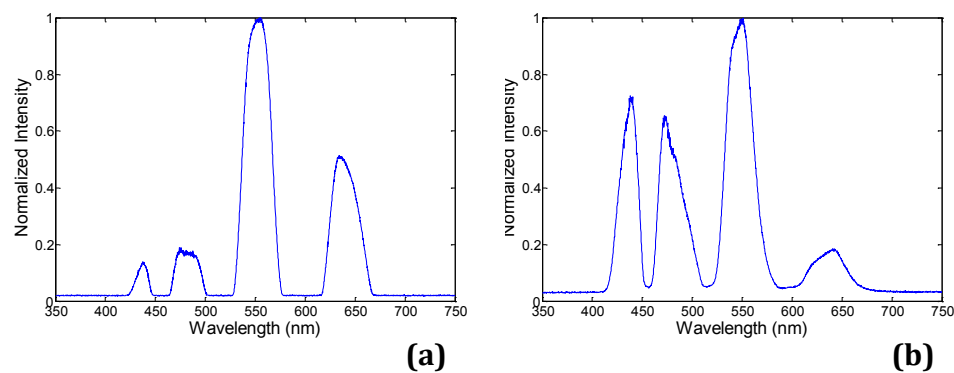


Figure 3.4 The spectra of (a) a copper reference grid, and (b) a sample of silver nanowires that are affected by the interference

We also performed simulations using Fourier optics analysis. Given the fact that the coherent light spot reflected by the DMD and the focused spot at the end of the fiber are Fourier transform pairs, we simulated the formation of the focused spots at the fiber end at various wavelengths for the unmodified DMD patterns, and the results are shown in Figure 3.5 (a)-(d). In each figure, the red circle indicates the region of the fiber end, where the optical signal can be coupled into the fiber and the spectrometer for the spectrum measurement. The light outside this region cannot be captured. The simulated results show that at some wavelengths, e.g. 530 nm in Figure 3.5(a) and 590 nm in Figure 3.5(c), the focused light spots on the Fourier plane of the image are totally outside of the region of the fiber end. For these wavelengths, the information is lost in the measured spectra. Figure 3.5 (d) displays the combined spot of 10 discrete wavelengths between 400 nm and 700 nm. As different wavelengths form the spots at different positions, only some of them can be coupled into the fiber, while the others are lost.

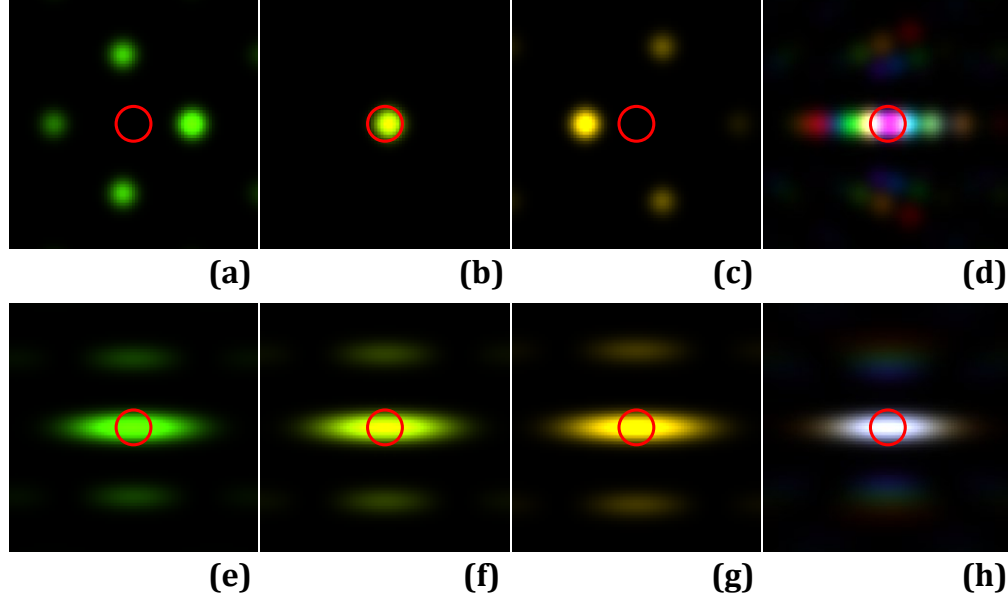


Figure 3.5 The simulated focused spots formed on the Fourier plane of the image at (a) 530-nm, (b) 560-nm, and (c) 590-nm wavelengths, using unmodified DMD patterns; (d) the focused spot formed by a combination of 10 discrete wavelengths between 400 nm and 700 nm, using unmodified DMD patterns; the focused spots at (e) 530-nm, (f) 560-nm, and (g) 590-nm wavelengths, formed by modified DMD patterns; and (h) the focused spot formed by a combination of 10 discrete wavelengths between 400 nm and 700 nm, using modified DMD patterns. The red circles indicate the the region of the fiber end.

In order to avoid the distortion of the spectrum caused by the interference, the original DMD patterns are modified with an additional striped modulation pattern, as shown in Figure 3.6. Each column of the white stripe in Figure 3.6 (right) is one column of micro-mirrors reflecting light to the spectrometer. The distance between adjacent white stripes is made larger than the diffraction-limited spot diameter $d_s = 48.55 \mu\text{m}$, so that each coherent light spot on the image plane is reflected by only one column of the micro-mirrors at a time. Because the micro-

mirrors in the same column are exactly in the same plane when tilting at $+12^\circ$, no destructive interference will occur at the end of the coupling fiber for any wavelengths. The simulation results of the focused spots using the modified DMD pattern in Figure 3.5 (e)-(h) also verify the conclusion. All the spots at different wavelengths cover the region of the fiber end and can be measured by the spectrometer.

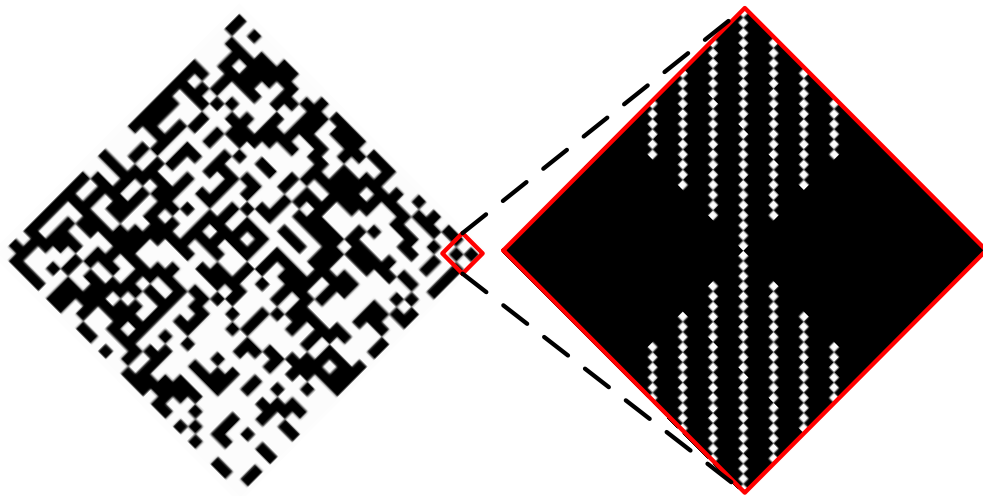


Figure 3.6 A modified 1024-pixel (32×32) binary pattern with an additional striped modulation pattern

Using the modified patterns, correct spectra can be achieved for the same LED-illuminated samples used in Figure 3.4, as plotted in Figure 3.7.

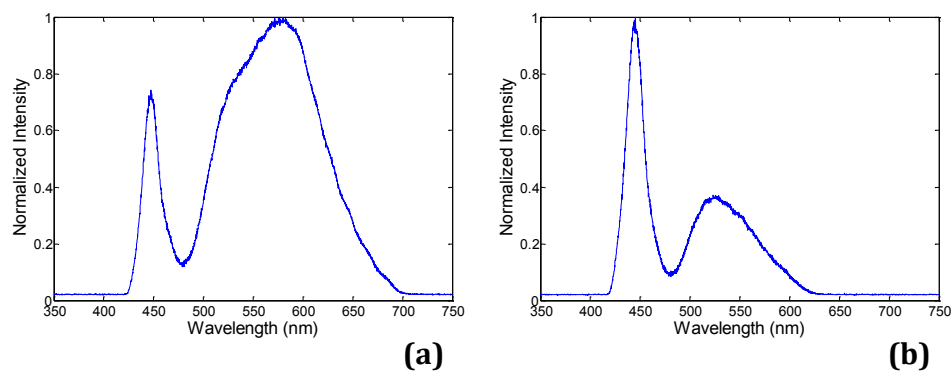


Figure 3.7 The spectra of (a) a copper reference grid, and (b) a sample of silver nanowires measured with modified DMD patterns.

Chapter 4

Experimental Results

In this chapter, we demonstrate the results of applying our compressive hyperspectral microscopy system on various objects including a standard resolution target and multiple surface plasmonic nanostructure samples. The performance of the actual system is analyzed, and the effects of noises on the reconstructed hyperspectral data are discussed. The compressively measured and recovered results are also compared with raster-scanning results in both spatial and spectral domain.

4.1. 1951 USAF Standard Microscope Resolution Target

The imaging system and the reconstruction algorithm were tested with a 1951 USAF standard microscope resolution target. The test target is a glass slide with patterned chromium coating on it. The elements in group 7 of the test target

was imaged at 16384-pixel (128×128) resolution ($N=16384$). A set of full measurements was applied by projecting the magnified image onto 16384 DMD modulation patterns and collecting the spectrum of the focused light from each modulated image. Figure 4.1 (a) plots a sequence of the measurement outputs at 637.44-nm wavelength. The pseudo-random binary patterns reflect 50% of the total pixels to the spectrometer, so the values in the measured sequence are fluctuating around the average. The images have been reconstructed at various sampling ratios M/N , where M is the amount of measurements actually used for the recovery of the image, and N is the total number of image pixels. Compression ratio N/M is the inverse of the sampling ratio. The curve of peak signal-to-noise ratios (PSNRs) of the recovered images versus sampling ratios is shown in Figure 4.1 (b). For a 637.44-nm single-band image slice in the hyperspectral data cube, the reconstruction with only 5% of all measurements achieves a PSNR of about 18 dB, and 25% measurements produce a reconstruction image with a 30-dB PSNR. The insets in Figure 4.1 (b) show the 128×128 images reconstructed at 10%, 25%, and 50% sampling ratios.

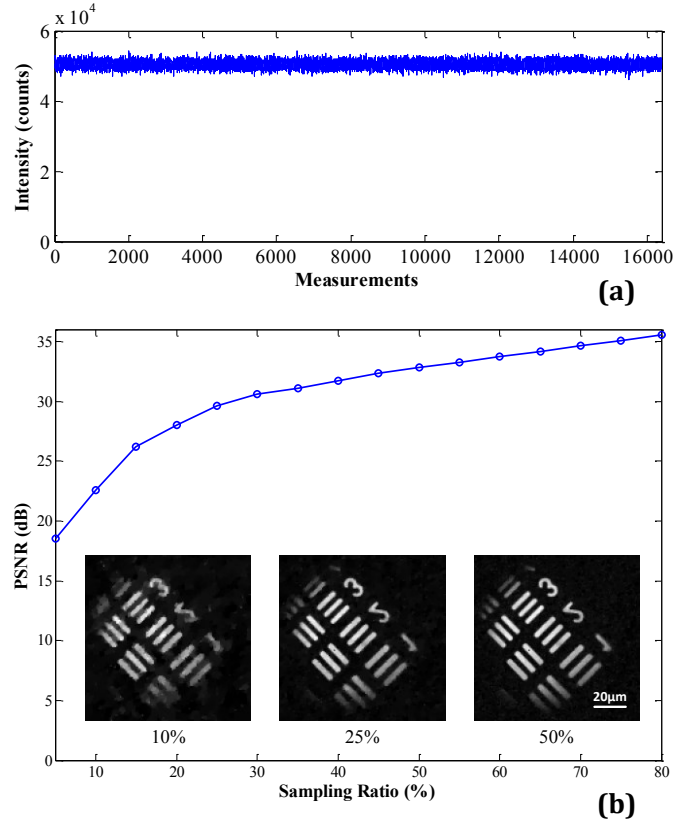


Figure 4.1 A 1951 USAF resolution target is imaged at 16384-pixel (128×128) resolution with the compressive hyperspectral microscopy system. The image slice at 637.44-nm wavelength is reconstructed at different sampling ratios. (a) A full set of compressive measurement results at 637.44-nm wavelength with a bandwidth of 1.52 nm. (b) The peak signal-to-noise ratio (PSNR) of the recovered images as a function of the sampling ratio (M/N). The insets show the images recovered from 10%, 25%, and 50% of the total measurements.

4.2. Hyperspectral Imaging of Nanostructure Surface Plasmon Scattering

To study the potential of the compressive hyperspectral imaging in the spectroscopic research on plasmonic nanostructures, we tested the system with the samples of gold nanobelts. The gold nanobelts have sub-100-nm rectangular cross

sections, and exhibit a strong transverse plasmon resonance peak at visible wavelengths [37]. The resonance peak of an individual gold nanobelt tunes with its cross-section aspect ratio, which is defined as the nanobelt width divided by the height. This plasmon resonance tuning can also be observed on one single gold nanobelt with a changing aspect ratio along its length. With the CS hyperspectral microscopy, such phenomenon can be efficiently observed.

The samples used in the experiments were prepared by depositing the gold nanobelts on glass substrates. Every nanobelt sample was imaged twice at 16384-pixel (128×128) resolution, with the polarizer positioned perpendicular and parallel to the nanobelt respectively. The integration time of the spectrometer for each measurement was set as 100 ms. And a total number of 4800 spectra were measured using 4800 DMD modulation patterns for one compressive hyperspectral imaging. Using all or part of 4800 measurements, we can demonstrate the reconstructions with sampling ratios below 29.3%, or equivalently compression ratios above 3.41. The imaged wavelength range spanned from 450 nm to 900 nm, and was divided into 300 bands, with an average bandwidth of 1.51 nm for each band.

Figure 4.2 (a)-(d) show the experimental results of 4 gold nanobelt samples. On top left of each figure is the color CMOS camera image of the nanobelt of interest. The scattered light from all four of them has notable color variation along their lengths. The hyperspectral data of these samples are reconstructed at 25% sampling ratio. The spectra of 10 points along each nanobelt are extracted from the

reconstructed hyperspectral data, and are plotted in each subfigure in Figure 4.2. As indicated by the arrows in the CMOS camera images, the blue spectra are polarized transverse to the gold nanobelts, while the red spectra are polarized parallel to them. The strong transversely polarized plasmon resonances show blue or red shifts in accordance with the color changes in the camera images. The parallel polarized spectra do not show plasmon resonance modes within the visible or near infrared bands. 6 artificially-colored single band image slices between 550-nm and 700-nm wavelengths are also synthesized from the reconstructed data for each sample, and are illustrated in Figure 4.2. From these single-band images, we can also notice the intensity distribution variations between different wavelengths.

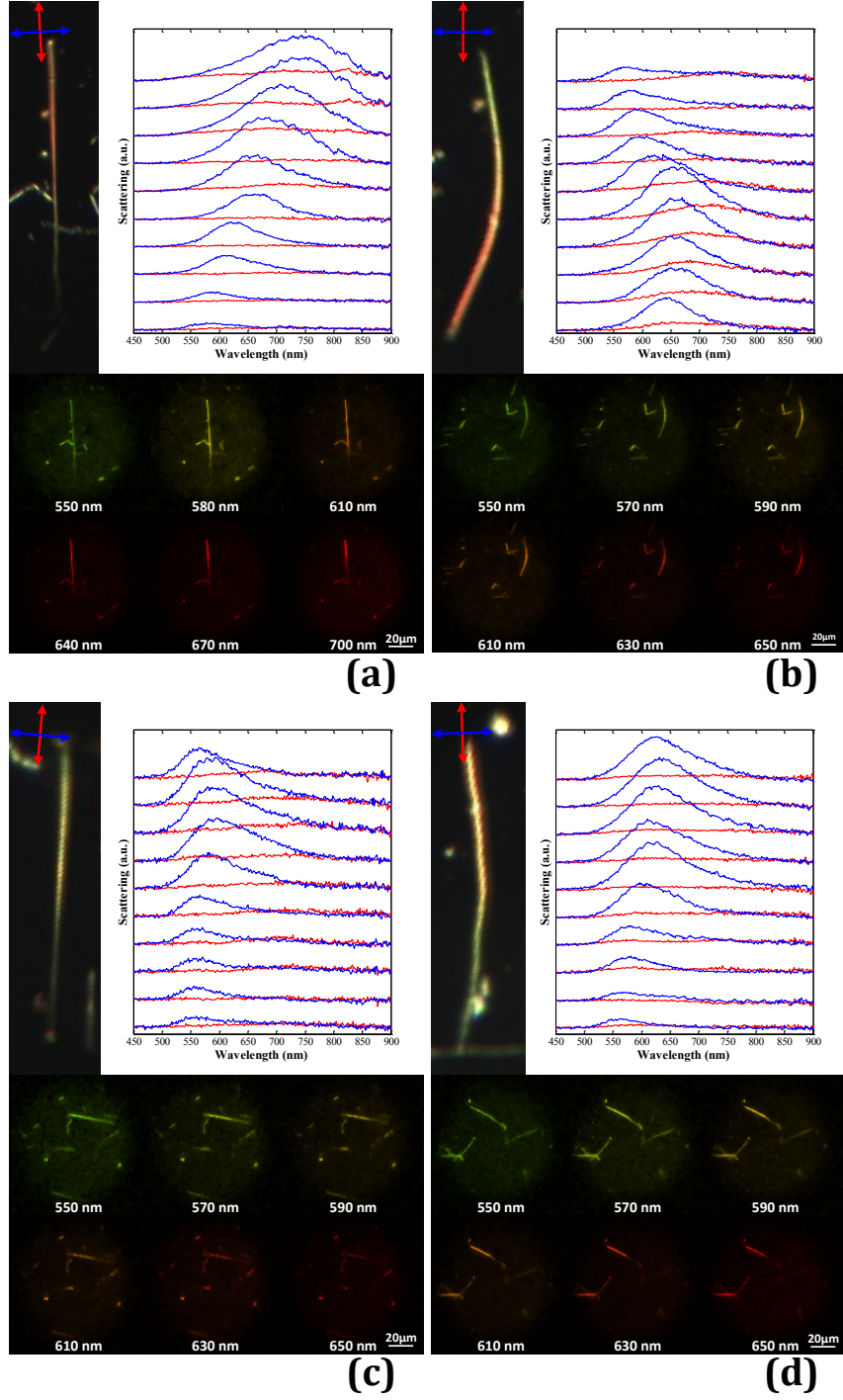


Figure 4.2 Examples of the reconstructed hyperspectral data of the gold nanobelt plasmon scattering at 25% sampling ratio. On top left of each subfigure is the cropped CMOS camera image showing the nanobelt of interest. The reconstructed spectra of 10 points along the nanobelt are plotted on top

right. And on the bottom of each subfigure are six synthesized single-band image slices from the reconstructed hyperspectral data cube.

4.3. Noise Analysis

The effect of noises in the system on the final reconstructed images was also studied analytically and experimentally. There are three major sources of noise that are introduced during the integration and read out of a spectrum from the QE65000 spectrometer, including the dark current noise, the photon noise, and the read noise. Because these noises and the image reconstruction can be considered independent between different bands, for simplicity, we just analyze the measurements at a single wavelength band.

The dark current noise is caused by the thermally generated electrons in the spectrometer sensors, producing a non-zero output on every band even when the spectrometer receives no input photons. It follows the Poisson distributions, and can significantly affect the measurements when the signal photon flux is at a similar level of the noise. In the analysis model, the dark current noise can be approximated with an additive Gaussian noise term e_d and an additional constant mean value μ_d . The constant mean value can be subtracted by a black frame. The standard deviation of the dark current noise is $\sigma_d = \sqrt{\mu_d}$.

The photon noise is the result of the random processes of signal photon detections that follow a Poisson relationship to the signal. It can also be approximated in the model with an additive Gaussian noise e_p with a standard

deviation σ_p proportional to the square-root of the signal. In the CS measurements, the signal level is around half of the scene light.

The read noise is a combination of noises that are independent to the signal level, including the on-chip noises and off-chip noises such as amplifier noise. It's a Gaussian distributed error term e_r with a constant standard deviation σ_r .

The overall model of the measurements with noises would be:

$$\mathbf{y} = \mathbf{\Phi}\mathbf{x} + \mathbf{e}_d + \mathbf{e}_p + \mathbf{e}_r \quad 3.1$$

where \mathbf{e}_d , \mathbf{e}_p , and \mathbf{e}_r are $M \times 1$ vectors with elements independently following the Gaussian distributions of e_d , e_p , and e_r , respectively. The effect of these measurement noise vectors on the final reconstructed image is complicated as it depends on the measurement patterns, the stability of the optimization algorithm, and the compression ratio. However, we can get a rough approximation by considering the case of a full measurement when $M=N$. Then the reconstruction is a complete inverse problem that can be simply expressed by

$$\hat{\mathbf{x}} = \mathbf{\Phi}^{-1}\mathbf{y} = \mathbf{x} + \mathbf{\Phi}^{-1}(\mathbf{e}_d + \mathbf{e}_p + \mathbf{e}_r). \quad 3.2$$

When $\mathbf{\Phi}$ is a permuted 0-1 Walsh-Hadamard matrix, as in our setup, the reconstruction error vector $\mathbf{\Phi}^{-1}(\mathbf{e}_d + \mathbf{e}_p + \mathbf{e}_r)$ yields a pixel-wise random error with a standard deviation

$$\sigma = \sqrt{\frac{4}{N}(\sigma_d^2 + \sigma_p^2 + \sigma_r^2)} \quad 3.3$$

where N is the number of image pixels.

In the experiments, with the illumination intensity kept at a constant level, we controlled the amount of signal photons collected by the detector by changing the integration time of the spectrometer. Reducing the integration time can largely increase the speed of the measurements, but it also affects the accuracy of reconstructions due to the decrease in the signal-to-noise ratio.

After going through the CS measurement and reconstruction, the independent noise distributions between the spectral bands cause a random fluctuation on the reconstructed spectrum of each pixel. So although a ground truth hyperspectral data set is hard to be achieved in the experiment, we can compare the noise levels by observing the levels of the fluctuation in the spectra.

Figure 4.3 illustrates the reconstructed spectra of a point on the gold nanobelt from the measurements with different integration time. The sample was imaged at 16384-pixel (128×128) resolution with a sampling ratio of 25%. The recovered spectra shown in Figure 4.3 (b) are normalized together to the maximum value in the spectrum with 100-ms integration time. All spectra start around 0.01, below which the photon signals are submerged by the dark current noise and read noise. With the increase of the integration time, the photon noise increases at the same rate of the square-root of the signal, and gradually exceeds the other noises. In Figure 4.3 (c), the spectra are normalized individually to their own peak values. An

intuitive comparison of the signal-to-noise ratio between different integration times can be performed by looking at the amplitude of the random fluctuations in the spectra. The spectra show a same plasmon resonance peak at 650 nm. However, the reconstruction from the measurements with only 10-ms integration time suffers more distortions because of the lower signal-to-noise ratio.

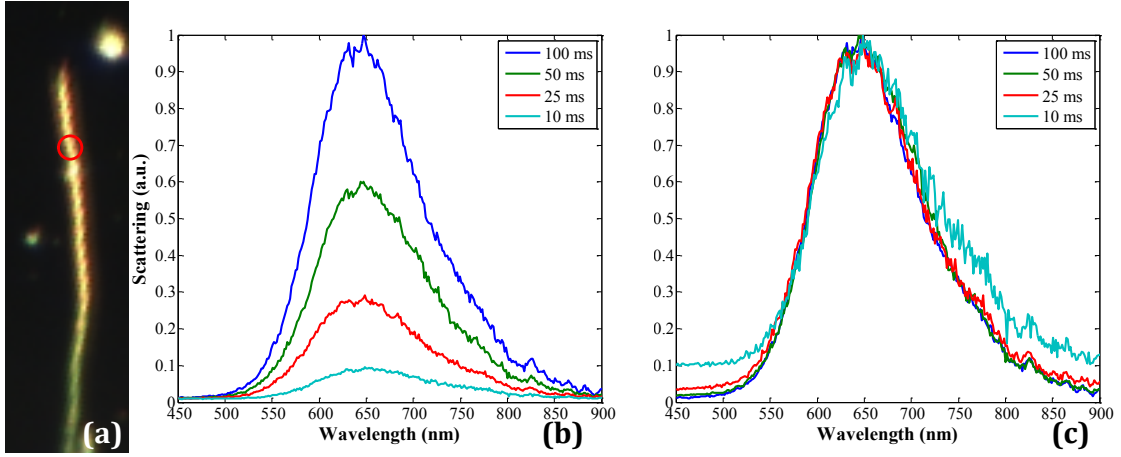


Figure 4.3 The reconstructed spectra from the measurements with different integration time. (a) CMOS camera image of the gold nanobelt. The red circle highlights the point where the spectra are plotted. (b) The reconstructed spectra of the high-lighted point with 100-ms, 50-ms, 25-ms, and 10-ms integration time. (c) The reconstructed spectra normalized to their own maximum values.

4.4. Comparison between Compressive Imaging and Raster Scanning

Raster-scanning based measurements with noises can be represented as

$$\hat{\mathbf{x}} = \mathbf{x} + \mathbf{e}_{d,raster} + \mathbf{e}_{p,raster} + \mathbf{e}_{r,raster} \quad 3.4$$

where $\mathbf{e}_{d,raster}$, $\mathbf{e}_{p,raster}$, and $\mathbf{e}_{r,raster}$ are the error vectors caused by dark current, photon, and read noises in the pixel-by-pixel measurements. Under the same illumination level and measurement condition, the standard deviations of the dark current noise and the read noise are the same as in the CS measurements, so $\sigma_{d,raster} = \sigma_d$ and $\sigma_{r,raster} = \sigma_r$. Without the pixel-multiplexing, the average photon noise is affected directly by the square-root of the pixel intensity, so $\sigma_{p,raster} = \sqrt{2/N} \sigma_p$. As a result, the overall noise on each pixel in the raster scanning method is

$$\sigma_{raster} = \sqrt{\sigma_{d,raster}^2 + \sigma_{p,raster}^2 + \sigma_{r,raster}^2} = \sqrt{\sigma_d^2 + \frac{2}{N} \sigma_p^2 + \sigma_r^2}. \quad 3.5$$

As revealed in the comparison between Equations 3.3 and 3.5, by multiplexing half of all the pixels in each measurement in the CS method, the dark current noise and the read noise in the image pixels are suppressed by a factor of $\sqrt{N}/2$. At 128×128-pixel resolution, these two types of noise can be reduced by 36 dB with the CS method. The pixel-multiplexing, however, increases the photon noise by a constant factor of $\sqrt{2}$, or 3 dB. Consequently, the CS method is especially useful in low-light, high-resolution imaging applications, including the hyperspectral microscopy.

To compare our experiment system with conventional scanning methods of hyperspectral imaging, we used the system to simulate a raster-scanning imaging process by changing the pseudo-random patterns to raster-scanning patterns. In each raster-scanning measurement, only the micro-mirrors inside a one-pixel patch

were activated to reflect light to the spectrometer, and the spectrometer output was directly stored as the spectrum of that pixel. The raster-scanning measurements were taken at 256-pixel (16×16), 1024-pixel (32×32), and 4096-pixel (64×64) resolutions. The CS measurements were taken at 4096-pixel (64×64) and 16384-pixel (128×128), with the sampling ratios of 50% and 25% respectively. All the spectra were measured with both 25-ms and 100-ms integration time under the same illumination condition.

The comparison of the results is shown in Figure 4.4. Using the raster-scanning method, the SNR drops drastically with the increase of the image resolution, because the average light intensity received by the spectrometer in each measurement is proportional to the pixel size. As seen in the second column of the images in Figure 4.4, the raster-scanning image with the resolution of 16×16 and 25-ms integration time roughly shows the illuminated region. Because of the low resolution, no detailed shapes of the nanostructures can be observed. The 32×32 raster-scanning image shows some more detailed structures, but the increase of the relative noise level greatly affects the image quality. And the 64×64 raster-scanning image becomes so noisy that most of the nanostructures cannot be distinguished. Increasing the integration time to 100 ms or more could improve the image quality, but also prolongs the measurement process. And the dependence of SNR on the pixel size in the raster-scanning method still prevents the acquisition of higher-resolution images.

In contrast, when the image is modulated by the permuted Walsh-Hadamard patterns of different resolutions in the CS method, the spectrometer always receives about 50% of the total light intensity from the whole field of view. As a result, the SNR of the measurements is much higher than that in the raster-scanning method, and does not decrease with the increase of the target image resolution. As shown in the 64×64 and 128×128 resolution 550-nm single band images acquired with CS method in Figure 4.4, the enhancement in the measurement SNR is also reflected in the quality of the final reconstructed images in the hyperspectral data cube.

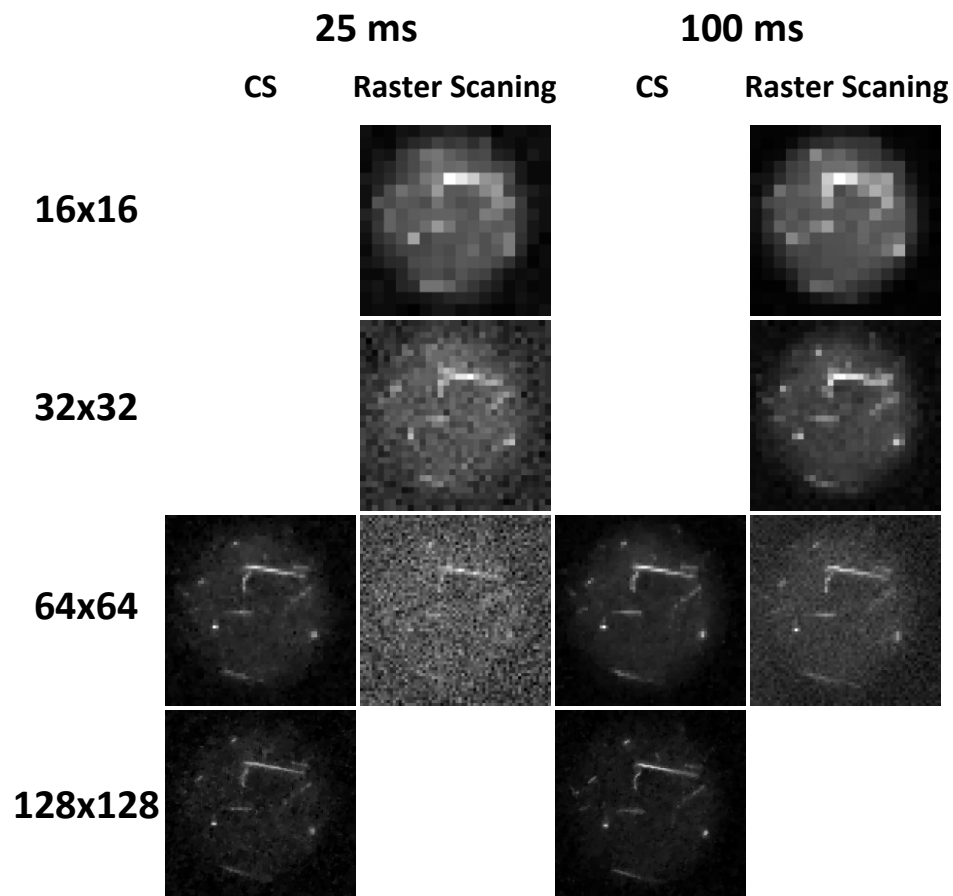


Figure 4.4 The single band images of the gold nanobelt sample at 550-nm wavelength acquired with CS and raster-scanning hyperspectral imaging methods.

Figure 4.5 plots the spectra of a bright point on one nanobelt, acquired with two different methods at same resolution of 64×64 and with same integration of 25 ms. It illustrates a ~ 15 -dB SNR improvement in the compressive imaging scheme in the spectral dimension of the hyperspectral data. It's the result of a combination of dark current and read noises reduction and the 3 dB photon noise increase.

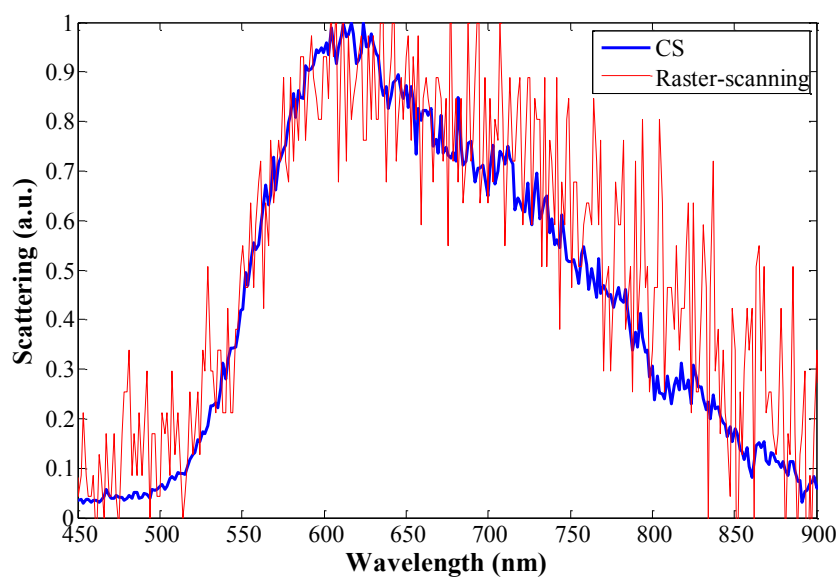


Figure 4.5 The spectra on pixel (18, 30) of the hyperspectral data cube acquired with CS and raster-scanning methods at the 64×64 resolution. The spectrometer integration time is 25 ms.

Conclusion and Future Work

In this thesis, we illustrate our design of a hyperspectral microscopy system based on the compressive sensing theory, and explore the diffractive effect of the DMD in an optics system with a diffraction-limited spot size much larger than the size of one micro-mirror. The DMD patterns are modified to solve the spectra distortion caused by the DMD diffraction and interference. Experimental results show the correct reconstructions of polarized SPR scattering spectra of gold nanobelts with different cross-section aspect ratio. The reconstructed hyperspectral data achieves a resolution of 128×128 pixels in spatial domain and 300 bands in spectral domain, covering the wavelength range from 450 nm to 900 nm with a 1.51-nm width for each band.

In addition to the pseudo-randomly permuted Walsh-Hadamard measurement matrix we applied in our experiments, there are some novel measurement matrices that introduce multiple benefits to the compressive

reconstructions. For example, the sum-to-one (STO) transform provides a multi-scale reconstruction strategy. It allows the images to be reconstructed at a lower resolution with no compression or at a higher resolution compressively, with the same set of measurements. The flexibility of this framework allows us to reduce the motion blur in the high-resolution reconstructions of moving objects by using the high-framerate low resolution reconstructions as previews. With this method utilized, we may be able to capture 4-D hyperspectral video data on our system.

Recently, the study on using the circulant matrix in compressive imaging enables an alternative design of the CS imaging system that does not need the use of a DMD. By replacing the DMD with a scanning mask in our system, the interference phenomenon caused by the tilted-mirror arrays on DMD will automatically disappear, and the efficiency of light collecting and coupling into the fiber will also increase without using the modified patterns.

References

- [1] K. Seekell, M. J. Crow, S. Marinakos, J. Ostrander, A. Chilkoti, and A. Wax, "Hyperspectral molecular imaging of multiple receptors using immunolabeled plasmonic nanoparticles," *Journal of biomedical optics*, vol. 16, pp. 116003-11600312, 2011.
- [2] J. Aaron, N. Nitin, K. Travis, S. Kumar, M. José-Yacamán, L. Coghlan, *et al.*, "Plasmon resonance coupling of metal nanoparticles for molecular imaging of carcinogenesis in vivo," *Journal of biomedical optics*, vol. 12, pp. 034007-034007-11, 2007.
- [3] C. P. Byers, B. S. Hoener, W.-S. Chang, M. Yorulmaz, S. Link, and C. F. Landes, "Single-Particle Spectroscopy Reveals Heterogeneity in Electrochemical Tuning of the Localized Surface Plasmon," *The Journal of Physical Chemistry B*, vol. 118, pp. 14047-14055, 2014.
- [4] R. A. Schultz, T. Nielsen, J. R. Zavaleta, R. Ruch, R. Wyatt, and H. R. Garner, "Hyperspectral imaging: a novel approach for microscopic analysis," *Cytometry*, vol. 43, pp. 239-247, 2001.
- [5] W. F. Vermaas, J. A. Timlin, H. D. Jones, M. B. Sinclair, L. T. Nieman, S. W. Hamad, *et al.*, "In vivo hyperspectral confocal fluorescence imaging to determine pigment localization and distribution in cyanobacterial cells," *Proceedings of the National Academy of Sciences*, vol. 105, pp. 4050-4055, 2008.
- [6] M. Kim, K. Chao, D. Chan, W. Jun, A. Lefcourt, S. Delwiche, *et al.*, "Line-scan hyperspectral imaging platform for agro-food safety and quality evaluation: system enhancement and characterization," *Transactions of the ASABE*, vol. 54, pp. 703-711, 2011.
- [7] P. J. Cutler, M. D. Malik, S. Liu, J. M. Byars, D. S. Lidke, and K. A. Lidke, "Multi-Color Quantum Dot Tracking Using a High-Speed Hyperspectral Line-Scanning Microscope," *PloS one*, vol. 8, p. e64320, 2013.
- [8] R. O. Green, M. L. Eastwood, C. M. Sarture, T. G. Chrien, M. Aronsson, B. J. Chippendale, *et al.*, "Imaging spectroscopy and the airborne visible/infrared imaging spectrometer (AVIRIS)," *Remote Sensing of Environment*, vol. 65, pp. 227-248, 1998.
- [9] M. B. Sinclair, J. A. Timlin, D. M. Haaland, and M. Werner-Washburne, "Design, construction, characterization, and application of a hyperspectral microarray scanner," *Applied optics*, vol. 43, pp. 2079-2088, 2004.
- [10] N. Gat, "Imaging spectroscopy using tunable filters: a review," in *AeroSense 2000*, 2000, pp. 50-64.
- [11] N. Hagen, R. T. Kester, L. Gao, and T. S. Tkaczyk, "Snapshot advantage: a review of the light collection improvement for parallel high-dimensional measurement systems," *Optical Engineering*, vol. 51, pp. 111702-1-111702-7, 2012.

- [12] M. B. Sinclair, D. M. Haaland, J. A. Timlin, and H. D. Jones, "Hyperspectral confocal microscope," *Applied optics*, vol. 45, pp. 6283-6291, 2006.
- [13] J. Hernandez-Palacios and L. Randeberg, "Intercomparison of EMCCD-and sCMOS-based imaging spectrometers for biomedical applications in low-light conditions," in *SPIE BiOS*, 2012, pp. 82150Q-82150Q-9.
- [14] T. C. George, D. A. Basiji, B. E. Hall, D. H. Lynch, W. E. Ortyn, D. J. Perry, *et al.*, "Distinguishing modes of cell death using the ImageStream® multispectral imaging flow cytometer," *Cytometry Part A*, vol. 59, pp. 237-245, 2004.
- [15] M. Gehm, R. John, D. Brady, R. Willett, and T. Schulz, "Single-shot compressive spectral imaging with a dual-disperser architecture," *Optics Express*, vol. 15, pp. 14013-14027, 2007.
- [16] L. Gao, R. T. Kester, N. Hagen, and T. S. Tkaczyk, "Snapshot image mapping spectrometer (IMS) with high sampling density for hyperspectral microscopy," *Optics express*, vol. 18, pp. 14330-14344, 2010.
- [17] L. Gao, R. T. Kester, and T. S. Tkaczyk, "Compact Image Slicing Spectrometer (ISS) for hyperspectral fluorescence microscopy," *Optics express*, vol. 17, pp. 12293-12308, 2009.
- [18] S. Dominguez-Medina, S. McDonough, P. Swanglap, C. F. Landes, and S. Link, "In situ measurement of bovine serum albumin interaction with gold nanospheres," *Langmuir*, vol. 28, pp. 9131-9139, 2012.
- [19] O. Neumann, A. S. Urban, J. Day, S. Lal, P. Nordlander, and N. J. Halas, "Solar vapor generation enabled by nanoparticles," *Acs Nano*, vol. 7, pp. 42-49, 2012.
- [20] C. Ayala-Orozco, C. Urban, M. W. Knight, A. S. Urban, O. Neumann, S. W. Bishnoi, *et al.*, "Au nanomatryoshkas as efficient near-infrared photothermal transducers for cancer treatment: Benchmarking against nanoshells," *ACS nano*, vol. 8, pp. 6372-6381, 2014.
- [21] E. J. Candès, "Compressive sampling," in *Proceedings of the International Congress of Mathematicians: Madrid, August 22-30, 2006: invited lectures*, 2006, pp. 1433-1452.
- [22] R. G. Baraniuk, "Compressive sensing," *IEEE signal processing magazine*, vol. 24, 2007.
- [23] E. J. Candès, J. Romberg, and T. Tao, "Robust uncertainty principles: Exact signal reconstruction from highly incomplete frequency information," *Information Theory, IEEE Transactions on*, vol. 52, pp. 489-509, 2006.
- [24] D. L. Donoho, "Neighborly polytopes and sparse solutions of underdetermined linear equations," 2005.
- [25] D. L. Donoho, "Compressed sensing," *Information Theory, IEEE Transactions on*, vol. 52, pp. 1289-1306, 2006.
- [26] Y. Zhang, "On theory of compressive sensing via l1-minimization: Simple derivations and extensions," *TR08-11, CAAM, Rice University*, vol. 27, 2008.
- [27] E. J. Candès and T. Tao, "Near-optimal signal recovery from random projections: Universal encoding strategies?," *Information Theory, IEEE Transactions on*, vol. 52, pp. 5406-5425, 2006.

- [28] H. Rauhut, "Stability results for random sampling of sparse trigonometric polynomials," *Information Theory, IEEE Transactions on*, vol. 54, pp. 5661-5670, 2008.
- [29] J. N. Laska, P. T. Boufounos, M. A. Davenport, and R. G. Baraniuk, "Democracy in action: Quantization, saturation, and compressive sensing," *Applied and Computational Harmonic Analysis*, vol. 31, pp. 429-443, 2011.
- [30] R. Baraniuk, M. Davenport, R. DeVore, and M. Wakin, "A simple proof of the restricted isometry property for random matrices," *Constructive Approximation*, vol. 28, pp. 253-263, 2008.
- [31] D. Goldfarb and W. Yin, "Second-order cone programming methods for total variation-based image restoration," *SIAM Journal on Scientific Computing*, vol. 27, pp. 622-645, 2005.
- [32] J. M. Bioucas-Dias and M. A. Figueiredo, "A new TwIST: two-step iterative shrinkage/thresholding algorithms for image restoration," *Image Processing, IEEE Transactions on*, vol. 16, pp. 2992-3004, 2007.
- [33] S. Becker, J. Bobin, and E. J. Candès, "NESTA: a fast and accurate first-order method for sparse recovery," *SIAM Journal on Imaging Sciences*, vol. 4, pp. 1-39, 2011.
- [34] C. Li, "An Efficient Algorithm for Total Variation Regularization with Applications to the Single Pixel Camera and Compressive Sensing," M.A. thesis, Rice University, 2010.
- [35] M. F. Duarte, M. A. Davenport, D. Takhar, J. N. Laska, S. Ting, K. F. Kelly, *et al.*, "Single-Pixel Imaging via Compressive Sampling," *Signal Processing Magazine, IEEE*, vol. 25, pp. 83-91, 2008.
- [36] D. Takhar, J. N. Laska, M. B. Wakin, M. F. Duarte, D. Baron, S. Sarvotham, *et al.*, "A new compressive imaging camera architecture using optical-domain compression," pp. 606509-606509, 2006.
- [37] L. J. Anderson, C. M. Payne, Y.-R. Zhen, P. Nordlander, and J. H. Hafner, "A tunable plasmon resonance in gold nanobelts," *Nano letters*, vol. 11, pp. 5034-5037, 2011.